Gas bubble dynamics in airlift photo-bioreactors for microalgae cultivation by level set methods

Matteo Neviani[1,2], Patrizia Bagnerini[1], Ombretta Paladino[2*]

[1] Department of Mechanical, Energy, Management and Transportation Engineering, University of Genoa

Via Opera Pia 15, 16145 Genoa, Italy;

[2] Department of Civil, Chemical and Environmental Engineering, University of Genoa

Via Opera Pia 15, 16145 Genoa, Italy

* <u>corresponding author</u> *e-mail address: paladino@unige.it (O. Paladino)*

Abstract

Coupled level set and CFD (computational fluid dynamics) methods are adopted in this work to track the moving gas-liquid interfaces in the riser of an external loop airlift photobioreactor (ALR) in which microalgae are used to produce biofuels and capture CO_2 from flue-gas. Modeling the behavior of gas bubbles is a crucial aspect for the fine-tuning of the operation of the reactor when inserted into a closed-loop biorefinery at the pilot-scale. The experimental data used for simulation were completely acquired or calculated from hydrodynamic experimental campaigns carried out on the ALRs. The rise, coalescence, and shape dynamics of the bubbles of the flue-gas are simulated in a rectangular domain representing the vertical section of the ALR riser. Different correction approaches, such as the conservative level set method (CLSM), are proposed to face the volume loss characteristic of LSM. Computational results evidenced strong agreement with the experimental data (bubble shapes and trajectories). The physically-based CLSM model was then effectively used for the fine-tuning of the multiphase flow regime inside the ALRs, suggesting operating conditions for the outdoor cultivation with Reynolds number = 10000 – 11000, Sherwood number between 1400 and 1800, and spherical-caps bubbles in the upper half of the riser, mildly churning the microalgae while avoiding damages to their cells.

Keywords: Airlift; CO_2 capture, bubble dynamics; level set method; biorefineries; microalgae

1. Introduction

Biofuels represent a key alternative to reduce the carbon footprint of the energy sector. They are particularly appreciated in the transport sector, as they allow the exploitation of existing distribution and transport infrastructures [1] without prolonging the supply times. Particular interest in recent years has been dedicated to biodiesel produced by microalgae, since these organisms feed on nitrogen and phosphorus, being therefore usable for the bio-fixation of liquid waste streams (wastewater) and, through photosynthesis, they can sequestrate CO_2 from exhaust gases from the combustion of biofuels themselves, thus being promising for use in closed cycle biorefineries [2]. They are able to achieve high lipid productivity and do not create competitiveness on land use and/or food in the synthesis of biodiesel [3].

This type of biofuel production is not yet widely applied for marketing [4] as microalgae provide low yields that are not compatible with the high productivity required [5]; besides, large-scale production requires oil extraction and transformation processes that significantly affect costs [6]. Interesting options are the biorefineries, where first/second generation biofuel production systems are coupled with the cultivation of microalgae within integrated plants [7]. To this end, at the ECPL laboratory of the University of Genoa, a pilot-scale biorefinery has been designed. It uses waste frying oil, microalgae, and lignocellulosic biomass for the combined production of biodiesel and syngas and their transformation into energy, with the aim to minimize waste streams and partially sequestering CO_2 from flue-gas [8]. The plant is divided into three main sub-processes: the first is the synthesis of biodiesel by transesterification, the second is the production of syngas by gasification of biomass added with crude glycerol, and the third, the most critical one, involves the cultivation of *Chlorella vulgaris* in airlift photobioreactors (ALRs). Microalgae are fed by the wastewater from the transesterification process rich in glycerol and by the flue-gas produced during the combustion of syngas.

Airlift photobioreactors are very flexible and have been investigated for microalgae nurture, with the aim of producing biofuels [9] and/or CO_2 sequestration. In this sense, ALRs, although more complicated to deploy, are flexible and markedly suitable to be incorporated into biorefineries and integrated power generation systems, due to the multitude [10,11] of process parameters that can be used to optimize their operation.

The present work deals with the multiscale simulation of the external-loop ALRs employed in the pilot-plant described in [8]. For the growth of microorganisms, airlift reactors are considered to be superior to both tubular bubble reactors and open ponds; it is possible to obtain very fast light/dark cycles and good mixing without high energy demand. However, bubble size is a pivotal aspect as it reflects itself on mass transfer. The optimization of the size and shape of the bubbles ensures a good mass transfer between gas and liquid and guarantees the recirculation of microalgae. Knowledge of the flow regime is thus a piece of crucial information to optimize processes inside ALRs. When biological reactants such as microalgae are used and bubble flow could damage the cells, the possibility to manipulate the flow regime of the bubbles during microalgae growth becomes a major goal. All this motivates the study and simulation of the phenomenon in detail.

The scope of this paper is the development of a model based on the Level Set Method (LSM) [12] for the simulation of the bubble dynamics in the ALR riser, as well as its verification and validation with the experimental data collected during some hydrodynamic tests. This modeling approach was chosen since it allows taking into account topology variations, i.e. the possibility of bubble coalescing and splitting. This is a significant aspect, as knowledge of the shape and trajectory of the rising bubbles is crucial to increase CO_2 exchange between exhaust gases and microalgae.

Moreover, the representation of the moving interfaces, i.e. the surfaces of the bubbles, is achieved with a continuous implicit function defined on the whole domain. This implies a simplification as the numerical calculation of a solution does not require the development of complicated algorithms for the reconstruction of the front.

The multiphase model, after validation, was used for the fine-tuning of the ALRs operating conditions for the outdoor cultivation tests.

2. Materials and methods

2.1. Experimental reactor & measurements

Four external loop airlift reactors (EL-ALRs) were designed and assembled to conduct an experimental campaign principally apt to gauge the main dynamic parameters [8] and to conduct a rigorous scale-up procedure [13] of the cultivation process. A sketch of one of the EL-ALRs, annotated with the main dimensions, is illustrated in Figure 1. The construction material is transparent PolyMethyl MethAcrylate (PMMA) as regards the riser and the downcomer and PolyVinyl Chloride (PVC) for the horizontal collectors. This choice is made since light availability and dark/light cycle alternation play a decisive role in algae cultivation.

Gas is vertically insufflated in the photobioreactor through a sparger made of a perforated metal plate coupled with a porous sponge as a diffuser, located on the base of the riser. The ratio between riser and downcomer diameters is 2.2, falling within the [1.0, 3.0] range recommended in literature as the optimum one for airlift bioreactor design [14]. The volume of each reactor amounts to 10.5 L.

For the hydrodynamic, mass transfer, and cultivation experimental campaigns, both compressed air and carbon dioxide were used as the gas phase and pumped inside the reactor. Water and water plus glycerol (coming from the transesterification process of oil) constituted the liquid phase, while the third solid phase, dispersed in water, was constituted by microalgae *Chlorella vulgaris*.

Temperature, pH, conductivity, and dissolved oxygen (DO) probes plus microcontrollers (B&C Electronics, Italy) were installed in the midsection of the lower collector; conductivity was also detected at the top of both the riser and of the downcomer (WTW multiparameter portable device 3630) during the hydrodynamic campaign.

Both gas pressure and consequently mean fluid velocity were varied in the hydrodynamic tests to evaluate optimal residence times. Tracing tests, as suggested in [15], hinging on the injection of NaCl in correspondence with the riser sparger, were executed to compute, through electrical conductivity measures, the mean liquid velocity in the reactor sections. Bubble count and evaluation of bubble shape and dimension were performed by image acquisition (CANON EOS20D camera equipped with a CCD sensor). pH measures were used during these tests as an indirect estimation of carbon dioxide dissolved in circulating water. The data thereby continuously collected were stored in a real-time, remotely accessible database, as the reactor was equipped with Memo HQ SCADA system [16].

Generally, temperatures around 15 - 25 °C seems suitable for most algal species, even those which are adapted to grow at colder temperatures [17]. However, since the temperature of the solution inside the photobioreactor can grow in outdoor conditions, during the summer season the implementation of a temperature controller is recommended, even if it was not necessary during the outdoor cultivation tests (carried out between May and June at latitude 44°18' N). Note that the airlift reactor is thought of as an element of a closed-loop cycle, receiving CO_2-rich flue gases as the input gas phase. It follows that there should not be issues of low temperature, so a cooling circuit can be used.

C. vulgaris can grow in a temperature range of 12 - 26 °C (optimal 18 - 24 °C), and ranges for pH of 6.8 - 10.5 (optimal 7.2 - 8.5). It can tolerate high CO_2 concentrations, up to18% (v/v), with satisfactory fixation and growth rates [18]. Moreover, it can use crude glycerol to increase its lipid content and growth rates [19]. In mixotrophic conditions, glycerol concentration can reach 5 - 10 g L^{-1}.

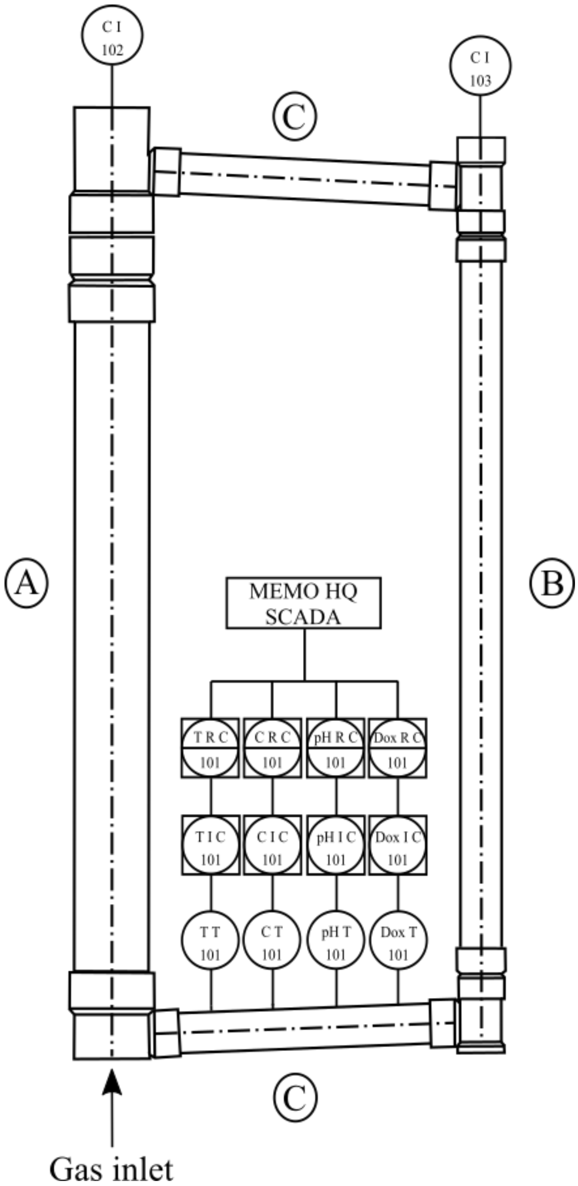

Figure 1. External loop airlift reactor: A – riser; B – downcomer; C – horizontal collectors.

In Table 1 the chemical-physical properties of the fluids are reported. The ALR dimensions and the dynamic parameters and operating variables measured during the experimental campaign are collected in Table 2. These data are used for simulation.

Table 1. Physical-chemical data used in the simulation.

Physical-chemical parameters	**Value**
Specific gas constant (CO_2)	188.9 J kg^{-1} K^{-1}
Surface tension coefficient (CO_2)	$72.86 \cdot 10^{-3}$ N m^{-1}

Liquid density (H_2O)	1000 kg m^{-3}
Liquid dynamic viscosity (H_2O)	$1.002 \cdot 10^{-3}$ Pa s
Gas dynamic viscosity (CO_2)	$1.47 \cdot 10^{-5}$ Pa s

Table 2. Data gathered in the experimental campaigns.

Geometric data	**Value**
Length of the riser	0.780 m
Diameter of the riser	0.110 m
Length of the downcomer	0.780 m
Diameter of the downcomer	0.050 m
Length of the horizontal collectors	0.385 m
Diameter of the horizontal collectors	0.050 m
Operating variables	**Value**
Temperature	293 K
Pressure	3 - 4 bar
pH	7.0 - 9
CO_2	15 - 20 %
NaCl pulse injection	1 - 10 g L^{-1}
Measured variables	**Value**
Gas velocity	0.57 - 0.64 m s^{-1}
Liquid velocity (in the riser)	0.06 - 0.14 m s^{-1}
Liquid velocity (in the downcomer)	0.17 - 0.39 m s^{-1}
(min, average, max) diameter of the bubbles	(0.003, 0.007, 0.020) m
Average number of bubbles in the riser	2200 - 2800

2.2. Mathematical modeling

The key role played by the hydrodynamics of the multi-phase flow for the proper operation of ALRs recommends detailed modeling of this aspect. In fact, it affects the shape and trajectory of the bubbles in the riser, which in turn significantly influences the mass transfer between gas and microalgae and hence the growth of the latter.

To build an appropriate model, two essential phenomena have to be taken into account: viscous fluid flow and moving interfaces, in addition to their mutual influence. Fluid flow is described by the non-dimensional form of the incompressible Navier-Stokes equations whereas interfaces are described through an implicit representation by resorting to the level set approach. The link between the two-equation systems is offered by the formulation of physical properties of the considered fluids, i.e. density ρ, dynamic viscosity μ and surface tension, all described as functions of the level set function ϕ.

The local formulation of the Navier-Stokes equations (NSE), obtained from momentum balance by resorting to the divergence theorem in conjunction with Reynolds transport theorem, is given by [20,21]

$$\rho \frac{\mathrm{D}\boldsymbol{u}}{\mathrm{D}t} = -\boldsymbol{\nabla} p + \left(\zeta + \frac{1}{3}\mu\right) \nabla(\nabla \cdot \boldsymbol{u}) + \mu \Delta \boldsymbol{u} + \boldsymbol{\xi} \qquad (1)$$

where the ratio $\mathrm{D}\boldsymbol{u}/\mathrm{D}t$ denotes the material derivative of the velocity $\boldsymbol{u}$. Moreover, ρ is the density, p the pressure of the fluid, μ the dynamic viscosity while ζ represents the volume viscosity (also known as second viscosity coefficient) and $\boldsymbol{\xi}$ other body forces (per unit volume) such as gravitational force per unit volume $\rho \boldsymbol{g}$.

As it is explained in the Supplementary Materials section S1, Eq. (1) can be non-dimensionalized as:

$$\frac{\mathrm{D}\boldsymbol{u}^\star}{\mathrm{D}t^\star} = -\boldsymbol{\nabla}^\star p^\star + \frac{1}{\mathrm{Fr}^2}\hat{\boldsymbol{e}}_g + \frac{1}{\mathrm{Re}}\Delta^\star \boldsymbol{u}^\star \tag{2}$$

where all the star superscripts indicate that the variables are non-dimensional, $\hat{\boldsymbol{e}}_g = \boldsymbol{g}^\star$, Fr is the Froude number, and Re is the Reynolds number.

The Level Set Method (LSM) is based upon a rather simple idea: the interface can be implicitly thought of as the zero iso-contour of a signed distance field $\phi(\boldsymbol{x}, t)$ called level set function (see Figure 2).

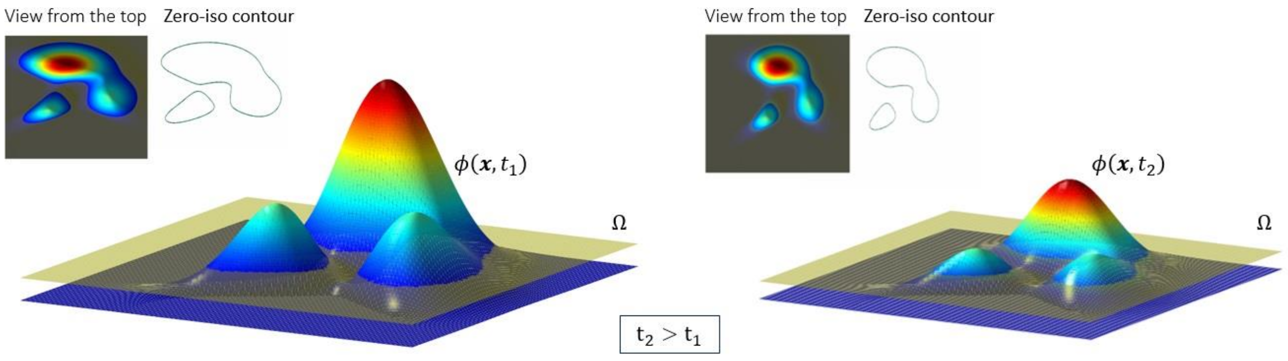

Figure 2. Illustration of the LSM.

Having called $\Omega \subset \mathbb{R}^n$ the space domain and T the final time, the level set function $\phi: \Omega \times [0, T] \to \mathbb{R}$ is the solution of the Hamilton-Jacobi equation

$$\begin{cases} \dfrac{\partial \phi(\boldsymbol{x}, t)}{\partial t} = \boldsymbol{u}(\boldsymbol{x}, t)\ ||\boldsymbol{\nabla}\phi(\boldsymbol{x}, t)|| \\ \phi(\boldsymbol{x}, 0) = \phi_0(\boldsymbol{x}) \end{cases} \tag{3}$$

where $||\cdot||$ is the Euclidean norm, $\phi_0: \Omega \to \mathbb{R}$ a given initial condition and $\boldsymbol{u}: \Omega \times [0, T] \to \mathbb{R}$ is the speed vector field. The zero level of ϕ_0 coincides with the initial location of the front and can therefore be set to the signed distance to it, meaning that the domain Ω is subdivided into two distinct regions Ω^+ and Ω^- ($\Omega^+ \cap \Omega^- = \emptyset$) by the boundary $\partial\Omega$ between Ω^+ and Ω^- ($\partial\Omega \notin \{\Omega^+, \Omega^-\}$), i.e. the zero level of ϕ_0.

$$\begin{cases} \phi(\boldsymbol{x}, t) > 0 & \boldsymbol{x} \in \Omega^+ \\ \phi(\boldsymbol{x}, t) = 0 & \boldsymbol{x} \in \partial\Omega \\ \phi(\boldsymbol{x}, t) < 0 & \boldsymbol{x} \in \Omega^- \end{cases} \tag{4}$$

The level set approach presupposes the computation of the latter at each time step, following the resolution of Eq. (3), to obtain the front propagation. However, an anticipated consequence of the convection term in Eq. (3) is the need for re-initialization of the distance profile, as a loss in the smoothness of field ϕ is to be expected. More details on the LSM can be found in section S2.

The link between the equations for the velocity field (NSE) and the interface tracking (realized thanks to an implicit representation obtained through the LSM) is offered by the formulation of the physical properties of the considered fluids (e.g. density and viscosity) as functions of the level set function ϕ. In this way, all the three essential elements (i.e. the velocity field, a description of the moving fronts and the coupling between interface tracking, and the velocity field) are effectively taken into account.

When multiphase flows are considered, jump discontinuities are commonly encountered across the fronts due to the diversity in those physical properties. The use of the smoothed Heaviside function $H_\varepsilon(\phi)$ allows the definitions of the density ρ and the kinematic viscosity ν of the two-phase flow system of incompressible fluids as:

$$\rho = \rho_g + \left(\rho_l - \rho_g\right) H_\varepsilon(\phi) \tag{5}$$

$$\nu = \nu_g + \left(\nu_l - \nu_g\right) H_\varepsilon(\phi) \tag{6}$$

being the subscripts g and l tags referring to the gas and liquid phases respectively. Another quintessential ingredient to model multiphase flows is the surface tension force (per unit length) $\boldsymbol{\xi}_{ST}$. In the context of front-tracking methods, the most widespread way to take into account such parameter is as a force concentrated on the interface [22], i.e.

$$\boldsymbol{\xi}_{ST}(\phi) = \sigma\kappa\hat{\boldsymbol{n}}\delta(\phi) \tag{7}$$

where σ is the coefficient of surface tension, $\hat{\boldsymbol{n}}$ is the normal vector of the moving interfaces, κ is the curvature, and, for computational purposes, one can use the mollified delta function $\delta_\varepsilon(\phi)$ instead of $\delta(\phi)$. This leads to a modified version of Eq. (2), as $\boldsymbol{\xi}$ needs to be updated as $\boldsymbol{\xi} = \rho\boldsymbol{g} + \sigma\kappa\hat{\boldsymbol{n}}\delta(\phi)$.

$$\frac{\partial \boldsymbol{u}^\star}{\partial t^\star} + \boldsymbol{u}^\star \cdot \boldsymbol{\nabla}^\star \boldsymbol{u}^\star = -\boldsymbol{\nabla}^\star p^\star + \frac{1}{\mathrm{Fr}^2}\hat{\boldsymbol{e}}_g + \frac{\sigma\kappa\hat{\boldsymbol{n}}\delta_\varepsilon}{\rho}\frac{\mathrm{L}}{\mathrm{U}^2} + \frac{1}{\mathrm{Re}}\Delta^\star \boldsymbol{u}^\star \tag{8}$$

2.3. Model implementation

The simulation framework was articulated in MATLAB environment, with a cascade model (Figure 3): a first resolution of the flow field modeled with the Navier-Stokes PDEs system and a second PDE, the Hamilton-Jacobi equation (Eq. (3)), handled to model the moving fronts related to the process described by the first PDEs system.

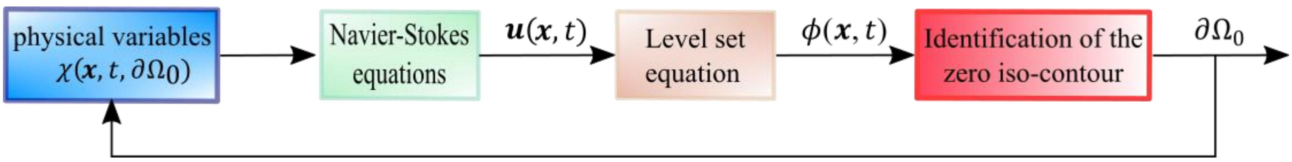

Figure 3. Numerical model schematization.

In particular, bidimensional NSEs in the non-dimensional form are solved by employing Chorin's projection on a Marker-and-Cell (MAC) staggered grid (Figure 4). The relative code is based on the NS solver programmed by Seibold [23] and utilizes a three-step semi-implicit scheme for time discretization (explicit treatment of the nonlinear convective term, implicit handling of the diffusive term, and pressure correction).

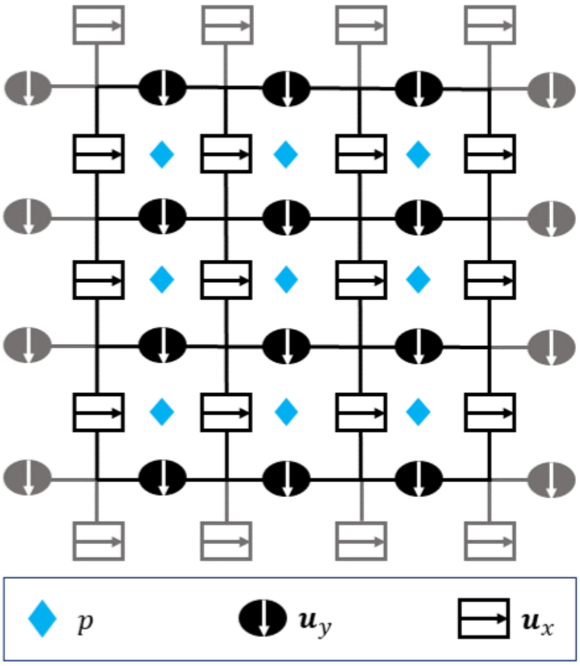

Figure 4. Staggered grid with boundary cells.

The portion concerning the resolution of the Hamilton-Jacobi equation for computing the zero level set was instead performed by using Mitchell's LSM toolbox [24]. The spatial discretization is performed by the means of an upwind second-order essentially non-oscillatory (ENO) scheme whilst time discretization is carried out with a 3-step, second-order total variation diminishing (TVD) Runge-Kutta scheme. The choice of upwind approximations is motivated by the hyperbolic nature of the PDE to avoid numerical instabilities. All PDEs were treated by relying on finite difference approximations.

The system equations were numerically solved in the spatial domain $\Omega = \left[-\frac{\mathrm{d_r}}{2}, \frac{\mathrm{d_r}}{2}\right] \times \left[-\frac{\mathrm{L_r}}{2}, \frac{\mathrm{L_r}}{2}\right]$, where $\mathrm{L_r}$ is the length of the ALR riser, equal to 0.78 m, and $\mathrm{d_r}$ is its diameter, equal to 0.11 m. Ω was discretized to form a mesh grid of rectangular cells, made up of 300 nodes in each dimension. Another possibility, whose results are reported in this work, consists of focusing on the bottom section of the airlift reactor, with the diffuser diameter (equal to the riser diameter) as the characteristic length. Since the collector diameter $\mathrm{d_c}$ is about half the riser diameter ($\mathrm{d_c}$ = 0.05 m), in this case, a square domain $\Omega = d_r \times d_r$ could better capture both bubble shape modifications and initial behavior in the inlet section, where the diffuser is highly influenced by the lateral collector. Referring for now to the first instance, i.e. Ω as a rectangular domain, the boundary conditions employed to evaluate the velocity field were of the Dirichlet type. No-slip conditions were imposed on three sides of the domain, both in the x and y direction. The right-side wall, on the contrary, was modeled to consider the inflow and outflow determined by the presence of the horizontal collectors. Hence, in correspondence with the openings, a noise-imposed, fairly flat profile velocity distribution typical of the turbulent fluid flow was adopted, while no-slip conditions were used elsewhere.

3. Results & discussion

3.1 Bubble shape and hydrodynamic regime

In order to maximize mass transfer, the maximum surficial area of exchange is required. It is also self-evident that, in a chosen surficial area, the longer the transport phenomenon lasts, the greater is the gain. This means that, in addition to needing suitable forms of the bubbles, it is also necessary to optimize their residence time in the riser, ensuring that appropriate trajectories are achieved. Hydrodynamics of multiphase flow thus holds a controlling influence on mass transport phenomena.

As long as the gas inlet velocity is maintained below a threshold value, dependent on the tube geometry, bubbles rise almost individually without significant interactions between them and with narrow bubble size distribution. In this flow condition, known as bubble or homogeneous flow, values of the diameter of the bubble d_b (taken equal to the diameter of a sphere having the same volume as the bubble) generally fall within the range of 1 - 6 mm. The ascent path is mostly rectilinear, with minor transverse and axial oscillations [25]. Whenever the gas phase velocity exceeds the aforementioned threshold, the density of the gaseous fraction in the liquid gradually increases, resulting in greater interaction between the bubbles, with collisions, clusters formation, and the occurrence of coalescence phenomena. The consequential appearance of larger bubbles significantly alters the hydrodynamic scenario, with the concomitant presence of large (about 20 mm) and small bubbles. These latter rises rather fast (1 - 2 m s^{-1}) stirring the liquid. The name of churn flow (also known as heterogeneous flow) is due to the fact that the larger bubbles tend to churn up the liquid [26]. In this state, as the corresponding Reynolds numbers prove to be higher (see Table 3), spiraling and zigzagging motions can be observed. Moreover, due to this rather turbulent environment, large bubbles often do not count on a clear definition of their form which rather fluctuates quite casually. Nevertheless, some characteristic shapes can be identified, since the morphology of the bubbles is mostly a function of the diameter, speed, and properties of the system. The work carried out by Grace [27] produced a well-known generalized graphical correlation (Figure 5) that depicts the individual geometry of a single rising bubble in terms of three dimensionless numbers: Reynolds number, Eötvös number Eo and Morton number Mo defined as

$$\mathrm{Eo} = \frac{g(\rho_l - \rho_g)d_b^2}{\sigma} \tag{9}$$

$$\mathrm{Mo} = \frac{g\mu_l^4(\rho_l - \rho_g)}{\rho_l^2\sigma^3} \tag{10}$$

Note that, in this context, the characteristic length required to compute Reynolds number is d_b.

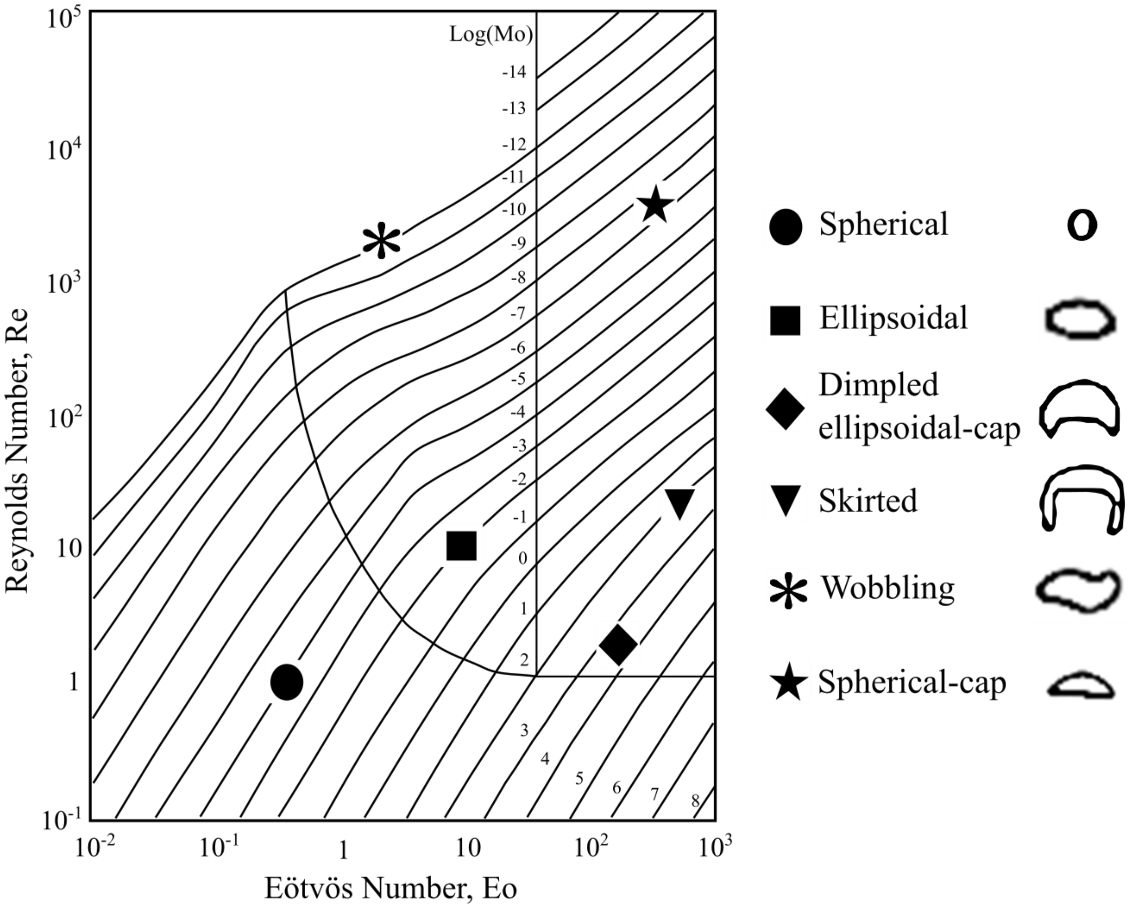

Figure 5. Grace's diagram [25]

By analyzing the diagram of Figure 5, oftentimes called Grace's diagram, one can surmise that the preferable shape is that of a spherical cap, given the high ratio between the exchange surface and the occupied volume. Proceeding with the reasoning, a zigzagging trajectory seems to be preferable, as it would extend the permanence time of the bubbles in the riser.

The experimental survey reported, in the chosen incipient churn regime, bubbles having an average mean diameter of 7 mm with shapes that varied from spherical, especially at the bottom of the riser (as it is to be expected since the orifices from which gas is introduced are circular), to spherical caps (Figure 6).

Table 3 summarizes the values of the main variables measured during the hydrodynamic experimental campaign and Table 4 reports the calculated variables and dimensionless numbers.

Table 3: Ranges of variables experimentally determined in ALRs.

Regime	Gas bubble velocity (m s^{-1})	Mean bubble diameter (mm)	Downcomer liquid velocity (m s^{-1})	Downcomer residence time (s)	Average time cycle (s)	Bubbles in the riser
Churn	0.573 – 0.642	5 – 7	0.168 – 0.235	3.5 – 4.8	20.4 – 27.6	1500-3000
Bubble	0.090 – 0.131	3 – 4	0.301–0.390	2 – 2.6	18 –24.7	3400-4000

Table 4: Ranges of variables calculated with empirical correlations and related dimensionless numbers in ALRs.

Regime	Riser liquid velocity (m s^{-1})	Re_{riser}	Re_{down}	Bubbles per cross-section
Churn	0.084 – 0.117	7865 –10955	9438 – 13202	15 – 35
Bubble	0.056 – 0.057	5244 – 5337	14543 – 18843	35 – 50

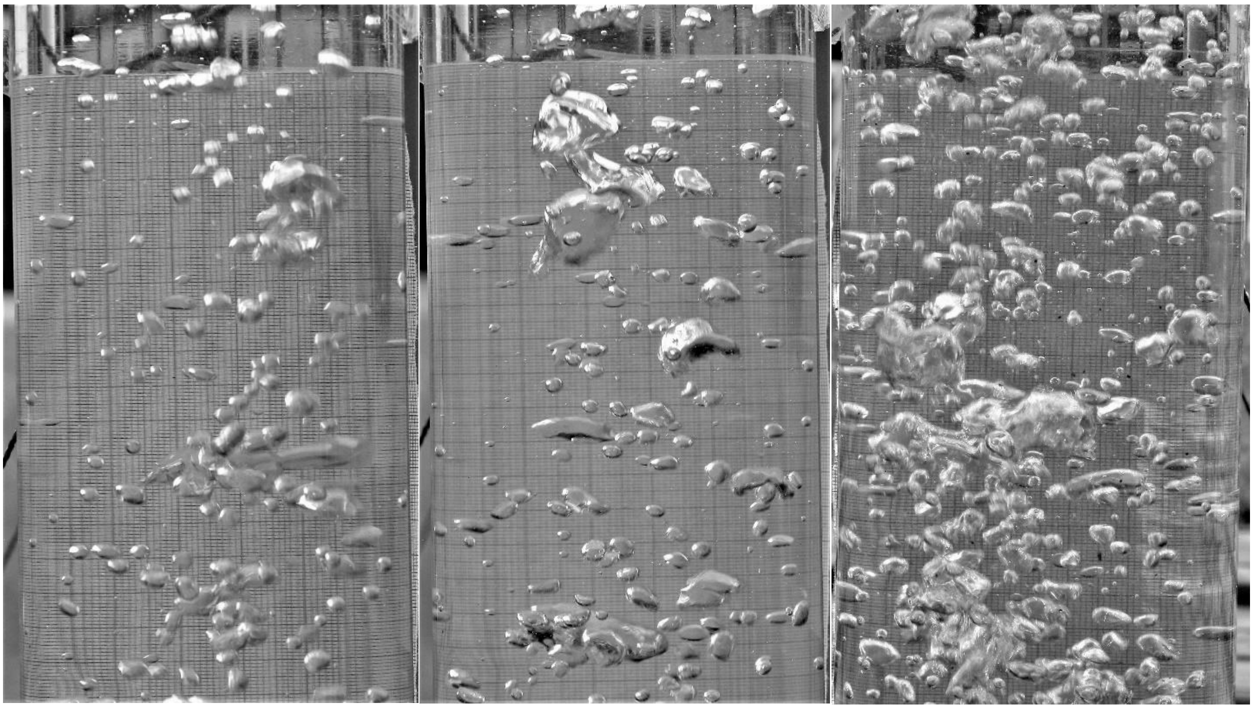

a b c

Figure 6. Bubbles in the riser from the experimental campaign in incipient churn flow: (a) bubble flow (gas bubble velocity = 0.12 m s^{-1}); (b) transition (gas bubble velocity = 0.35 m s^{-1}); (c) churn flow (gas bubble velocity = 0.62 m s^{-1})

3.2 Evaluation of gas-liquid mass transport coefficients:

Carbon dioxide contained in the flue-gas is the main substrate to microalgae needed for photosynthesis, while oxygen is the main product. We focalized here on CO_2 since the proposed multiphase model can describe in detail the behavior and the shape of the bubbles containing CO_2. The main goal in controlling the shape of the bubbles and their residence time is to increase mass transport between the bubbles and the liquid. Hence mass transport characteristics of the dissolved CO_2 to the suspended microalgae in the liquid phase should be optimized in the operation of the ALRs. The average mass flux of carbon dioxide to the microalgae is a function of the diffusion coefficient D ($m^2\ s^{-1}$) of CO_2 in water, the bulk concentration of CO_2 in water, the properties of the fluid (viscosity and density), the dimension of microalgae and their velocity with respect to that of the fluid.

The Sherwood number was calculated for the ALRs in the conditions reported in Table 5 as $\mathrm{Sh} = \frac{K_{0L} d_b}{D} = \frac{k_L a {d_b}^2}{D}$, where a ($m^2\ m^{-3}$) is the specific surface of the bubbles, d_b is the mean bubble diameter and k_L is the liquid global mass transport coefficient.

$k_L a$ can be experimentally estimated in ALRs using different correlations proposed in the literature. We adopted the following [28]:

$$k_L a = 0.79 \left(1 + \frac{A_{\mathrm{down}}}{A_{\mathrm{riser}}}\right)^{-2} u_{G,\mathrm{riser}}^{0.8} \qquad (11)$$

where A (m^2) is the cross-sectional area and u_G ($m\ s^{-1}$) is the gas velocity.

The values of $k_L a$ for the incipient churn regimes experimentally tested are in the range 0.15 - 0.30. The resulting Sh number ranges between 1200 and 3500. Since a can be also calculated as the product of the number of bubbles in the riser and the mean surface of the bubble divided by the volume of the riser, it results in a range of 7 - 15. The corresponding k_L is comprised between 0.01 and 0.04. The values of k_L related to the bubble regime and the fully developed churn regime also tested during this campaign, can be found in [13]. The optimal Sh number, calculated for the conditions reported in Table 5, and chosen for the outdoor cultivation tests, is in the range 1400 - 1800.

3.3. Simulation results using LSM

The overall computational model has been developed by gradually increasing the complexity of the simulated system: first, we followed a single bubble, then we considered multiple puffs of bubbles inserted in the computational domain at different times.

By virtue of the well-known volume loss problem by which the level set method is intrinsically affected, it has been necessary to introduce a correction apt to remedy such an issue. With a mere relocation of the level set function, lowered or raised according to need, using a simple algorithm based on the bisection method, the simulation resulted more than satisfactory, as it can be noticed in Figure 7. Substantially, one can exploit the fact that, provided that the scheme for the convection of ϕ is sufficiently accurate, the error on the volume balance in each time step should be very small. To avoid the error accumulation, which instead leads to the significant observed losses, it is thus advisable to apply the correction at each time step, at the same time paying attention not to alter the shape of the front. Presupposing a suitable rate of reinitialization of ϕ, in the proximity of the front, the level set function is the signed distance and therefore, in the vicinity of its zero iso-contour lines, ϕ presents level sets approximately equidistant to each other. Then, by translating ϕ upward or downward by a signed constant K, which represents the distance between the original level set and the one after the translation, the volume (or area in two dimensions) occupied by the gas is conserved and the shapes of the interfaces are essentially unaltered (Figure 8). For this method to be reliable, K must be small [29]. The algorithm counts the number of cells inside the interface at two successive times to judge if the latter has increased or decreased and therefore if it is necessary to lower or raise the zero-level set. The value of K is expected to be between zero and the maximum of the zero-level set, so one possibility is to use the bisection method within these two extremes.

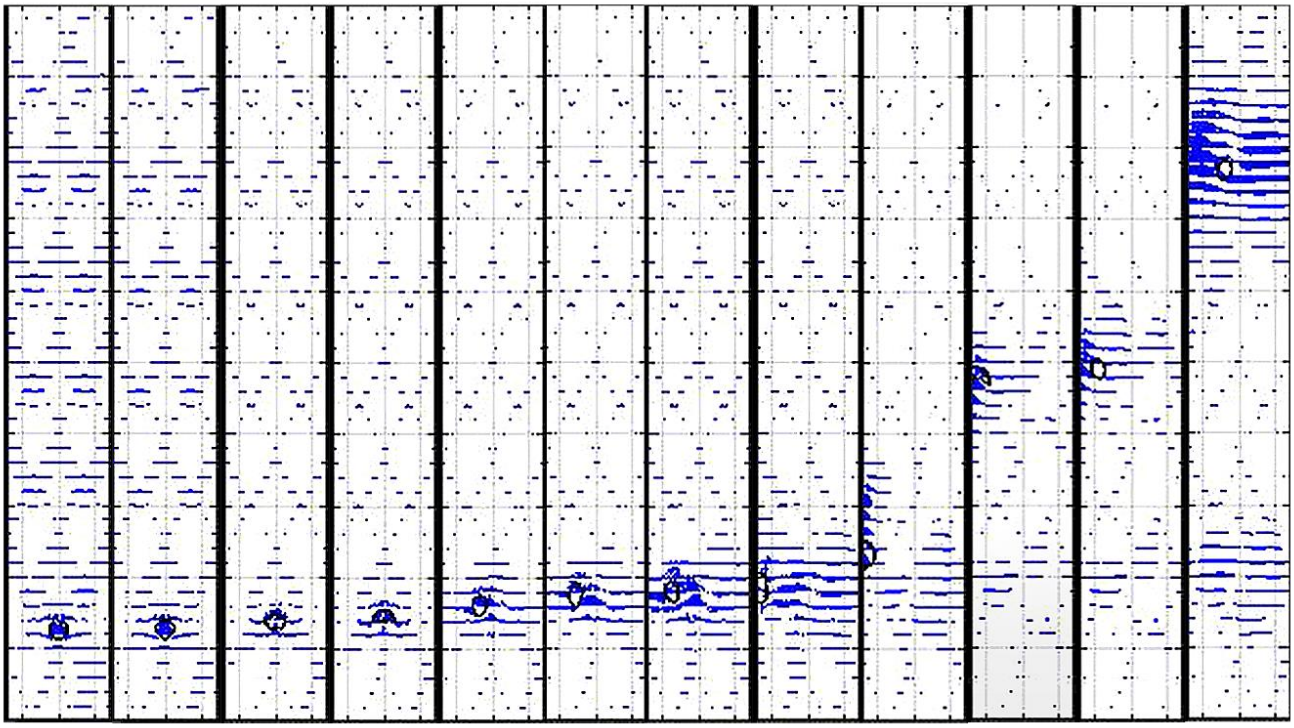

Figure 6. Simulation frames of the single bubble dynamic in the riser with LSM modified by the relocation of the level set function using the bisection method. On the background, the speed plot of the liquid velocity field; vectors are auto-scaled as to not overlap.

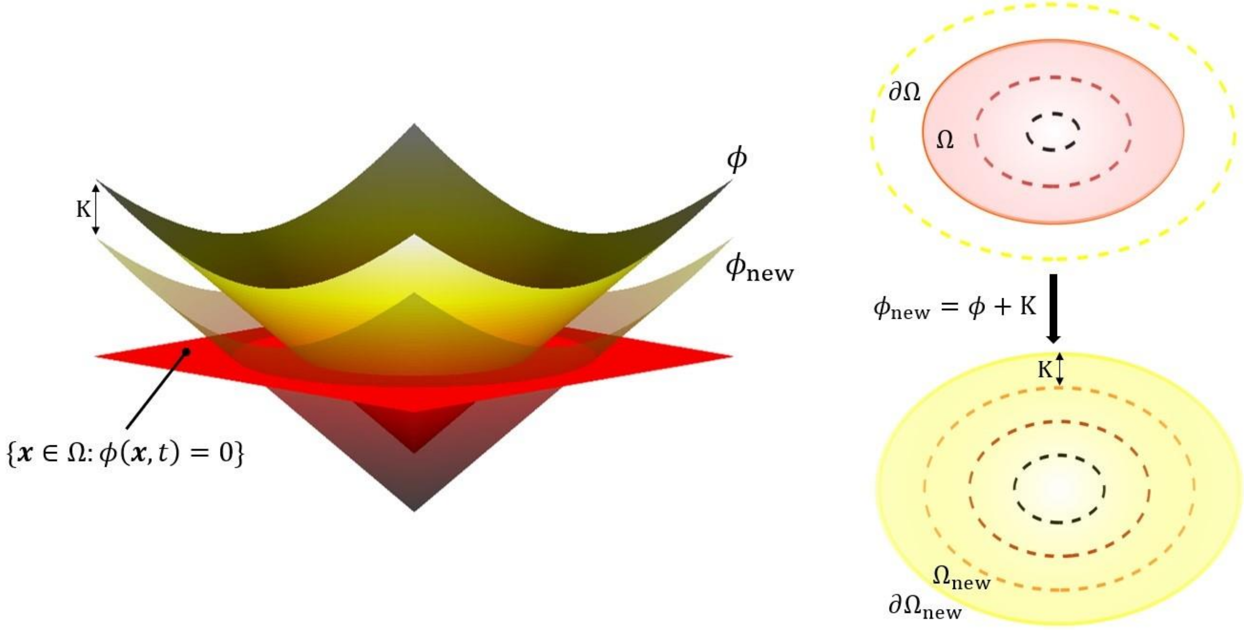

Figure 7. Level set correction by the relocation of the level set function ϕ, translated upward or downward by a signed constant K.

Although the precaution of inserting a correction on the balance of front volume worked just fine for the case of a single bubble, a further problem of distribution manifested in that of multiple bubbles: the number of grid cells standing within the fronts is preserved but the lost cells are typically added to the larger bubbles, without taking into account their position. The effect that follows is a sort of instantaneous transfer of matter, obviously devoid of physical meaning. It is possible to circumvent this issue (Figure 9) as long as one simulates the evolution of multiple bubbles that begin their walk at the same time and the frequency with which the correction is performed is suitably reduced [30]. Nevertheless, since this route is not feasible, it is necessary to implement a different approach. With this in mind, the adoption of the so-called conservative level set method (CLSM) [31,32] was decided.

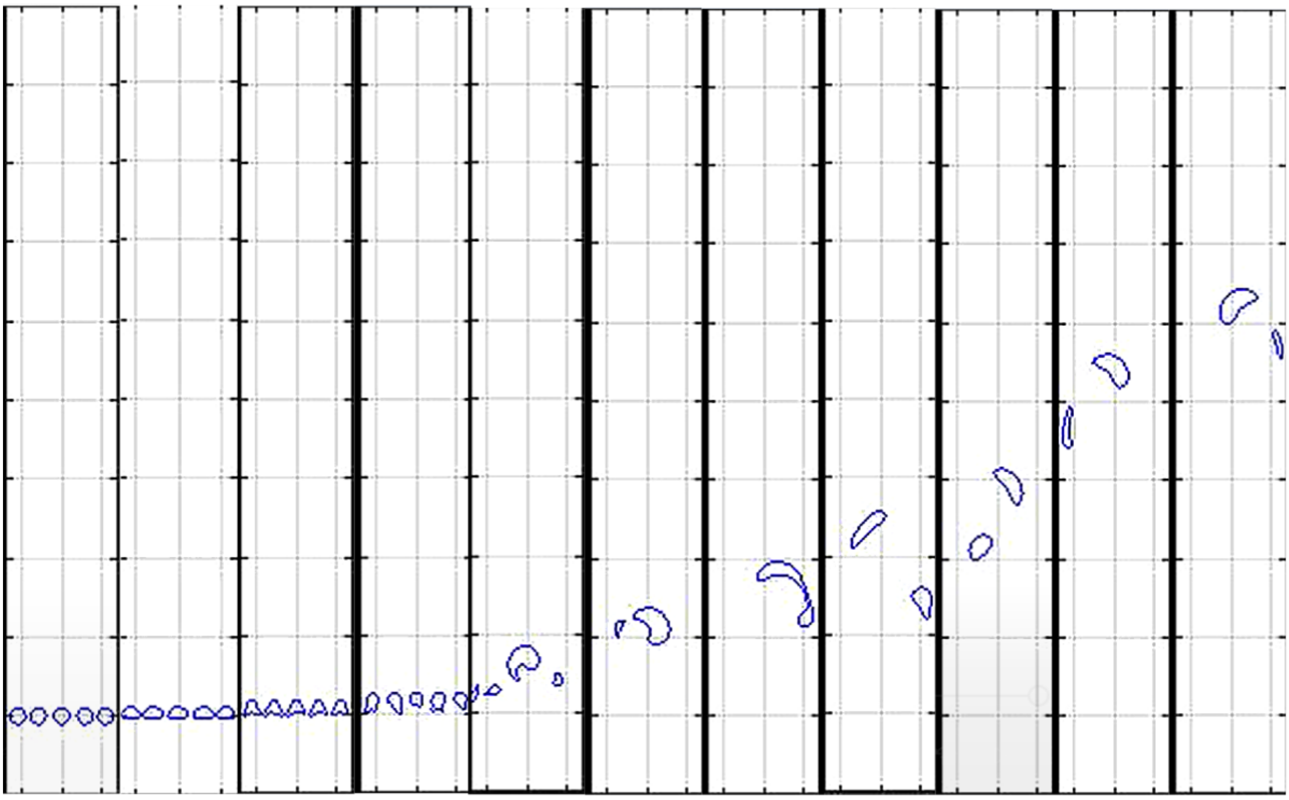

Figure 8. Simulation frames of instantaneous puff behavior for a 5 bubbles flow inside the riser, with LSM modified by the relocation of the level set function using the bisection method. To obtain a clearer and more understandable picture of bubble dynamics, the quiver plot has been disabled.

3.4. Simulation results using CLSM

CLSM entails the adoption of a different phase field function, employing ψ instead of ϕ, being $\psi(\boldsymbol{x},t) = H_\varepsilon(\phi(\boldsymbol{x},t))$. In this way, the position of the interface is implicitly represented, avoiding the need for computing both the step function and δ_ε. More importantly, if the advection of ψ is carried out in a conservative way, the volume bounded by the ½ iso-surface is approximately preserved (exactly if one uses H instead of H_ε, but numerical issues would arise due to the nature of the sharp interface).

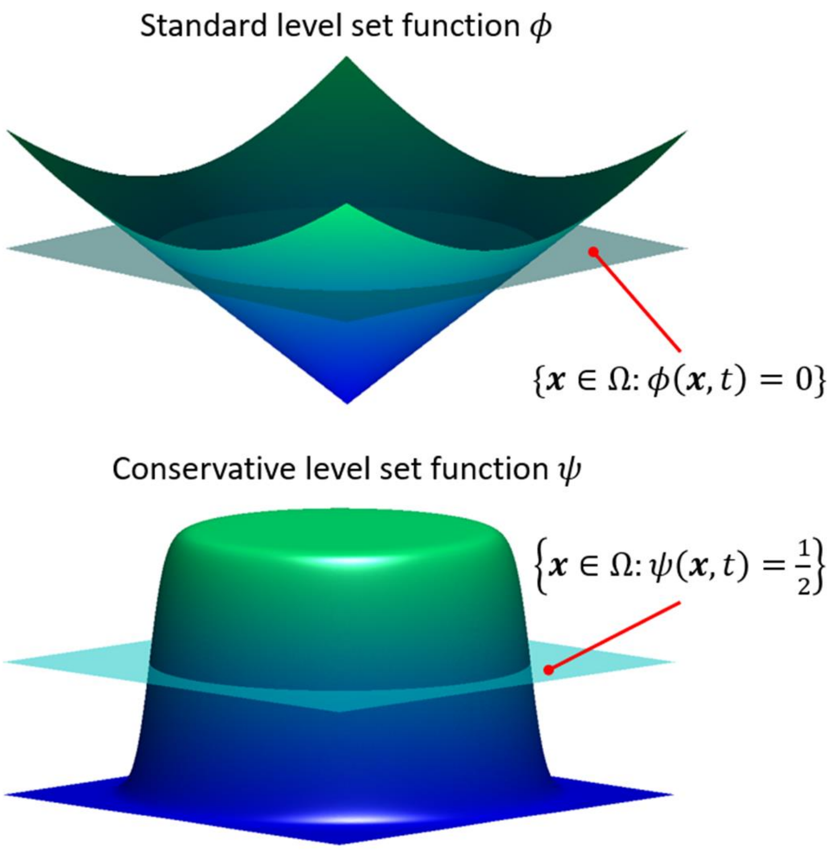

Figure 9. Comparison between standard LS (top) and Conservative LS (bottom) functions.

The function ψ is initialized as a hyperbolic tangent (Eq. (12)) of thickness ε as, for $\varepsilon \to 0$, it tends [33] to the exact Heaviside step function $H(\phi)$:

$$\psi(\boldsymbol{x}, t) = \frac{1}{1 + \exp\left(\frac{\phi(\boldsymbol{x}, t)}{\varepsilon}\right)} = \frac{1}{2}\left(1 + \tanh\left(\frac{\phi(\boldsymbol{x}, t)}{2\varepsilon}\right)\right) \tag{12}$$

The conservative level set method articulates in two steps. The first one, similarly to standard LSM, is the advection of the phase function, expressed as:

$$\frac{\partial \psi}{\partial t} + \boldsymbol{u} \cdot \boldsymbol{\nabla} \psi = 0 \tag{13}$$

which, in the presence of a divergence-free flow field, one can reformulate as:

$$\frac{\partial \psi}{\partial t} + \boldsymbol{\nabla} \cdot (\boldsymbol{u}\psi) = 0 \tag{14}$$

Eq. (14) is a conservation equation and as such lends conservation properties to the algorithm.

The second step is the reinitialization, needed to regularize the shape of ψ and enhance numerical robustness. It consists of the resolution of the hyperbolic PDE Eq. (15), comprised by a compressive limiter intended to sharpen the profile and a diffusive one in the normal direction, used to balance it and maintain the adequate interface thickness.

$$\frac{\partial \psi}{\partial \tau} + \boldsymbol{\nabla} \cdot (\psi(1-\psi)\hat{\boldsymbol{n}}) = \varepsilon \boldsymbol{\nabla} \cdot \big((\boldsymbol{\nabla}\psi \cdot \hat{\boldsymbol{n}})\hat{\boldsymbol{n}}\big) \tag{15}$$

The evolution equation Eq. (15), reported in conservative form, has to be solved to steady-state in an artificial time τ framework. Courant–Friedrichs–Lewy (CFL) condition ensues for both advection and re-initialization steps. In particular, when applying the artificial compression technique, Olsson and Kreiss [31] suggested that

$$\Delta\tau \leq \frac{\mathrm{C}(\Delta x)^2}{\varepsilon} = 2\mathrm{C}(\Delta x)^{1+d} \tag{16}$$

with Courant number C = 0.25, ε interface thickness and d either 0 or very small (e.g. 0.1) for complicated flows. There, mesh size Δx was assumed uniform. In this work, we chose to use $\min(\Delta x, \Delta y)$ instead of Δx when dealing with the CFL condition in the rectangular space domain whilst exactly Δx when Ω is a square. When implementing the CLSM, we adopted precisely this latter definition of Ω, for the reasons already explained in section § 2.3.

Besides, concerning the choice of the mesh size, a tradeoff between volume conservation and accuracy emerges: if on the one hand smaller ε (Eq. (17)) implies better volume preservation and compliance with the CFL condition, on the other, it entails a decrease in the order of accuracy.

Exceeding in setting ε to a small value can determine the formation of spurious oscillations, which in turn may damage the normal field by switching its direction.

$$\varepsilon = \frac{(\Delta x)^{1-d}}{2} \tag{17}$$

In their presentation of CLSM, Olsson and Kreiss [31] attacked this problem by resorting to a second-order TVD method with Superbee limiter; nevertheless, in this way, the overall accuracy of the method is affected [34]. As efficaciously explained by McCaslin & Desjardins [35], excessive re-initialization can damage the simulation results revealing equation stiffness. To relieve this degradation, Desjardins et al. [36] suggested a reconstruction of ϕ from ψ through the fast marching method (FMM), by which a smooth normal field is obtained. Anyway, instead of resorting to this algorithm, called accurate conservative level set (ACLS), we privileged simplicity over computational speed: we opted for a remapping of ψ by first restoring the steep profile of the Heaviside step function, and then smearing it out with a Gaussian filter (Figure 11) [37]. Since this causes volume loss, in order not to waste the benefits of using CLS, we coupled it with the correction by translation of the level set function already used in the LSM.

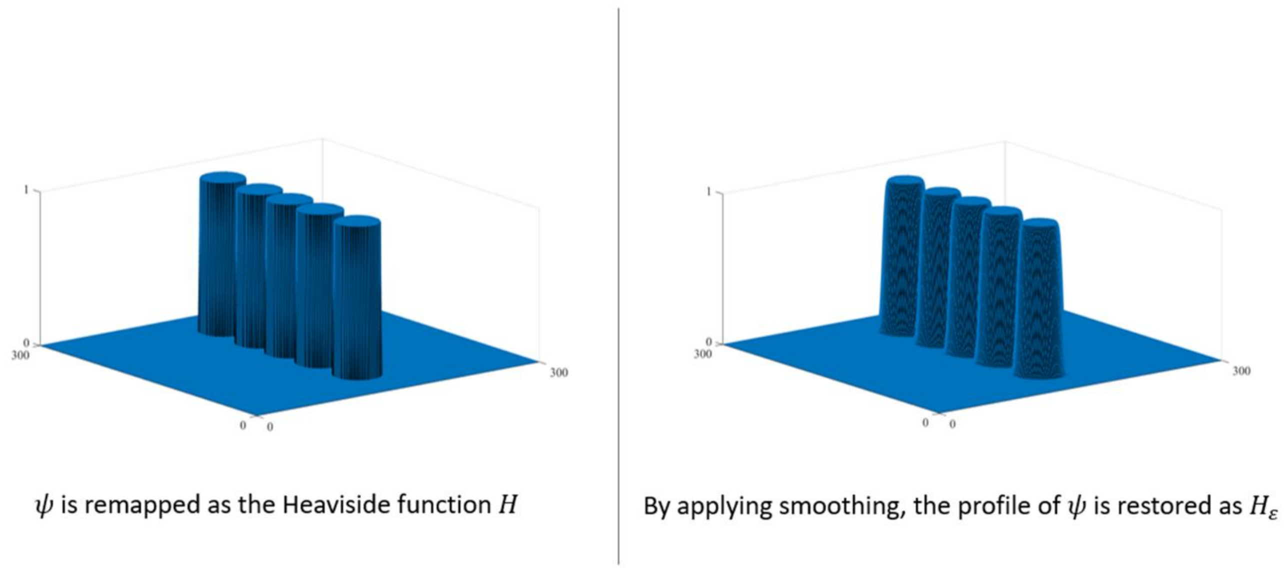

Figure 10: CLS function remapping.

Simulations were carried out on a regular square grid mad up by 300 × 300 points, as $\Omega = \mathrm{d_r} \times \mathrm{d_r}$, with Dirichlet boundary conditions for each edge of the computational domain. In particular, no-slip conditions were applied in both directions to the southern and western edges, to the upper half on the eastern boundary. The definition is instead trickier on the northern boundary. We opted to impose vertical component velocity of the same value as the mean liquid velocity measured experimentally in the riser $v_{L,\mathrm{r}}$ added with Gaussian White Noise (GWN, zero mean, $0.05 \cdot v_{L,\mathrm{r}}$ variance), whilst pure GWN was used to introduce small aleatory deviations in the x-direction. The same stratagem was employed to model the components of the imposed velocity profile on the eastern edge in the lower half (fluid coming from the horizontal collector). In particular, $\boldsymbol{u}_y$ is described as GWN and $\boldsymbol{u}_x$ the sum of mean liquid velocity in the collector $v_{L,\mathrm{c}}$ and GWN. The resulting velocity field, for one of the simulated diffuser positions, is depicted in Figure 12. The detail of some simulations with CSLM, representing the bottom section of the riser, are presented in Figure 13. Frames are reported with a frequency equal to 25Hz in order to better observe bubbles shape dynamics (the mean experimental gas velocity into the riser is in the range 0.4 – 0.8 m s^{-1} in incipient churn regime, see Table 3).

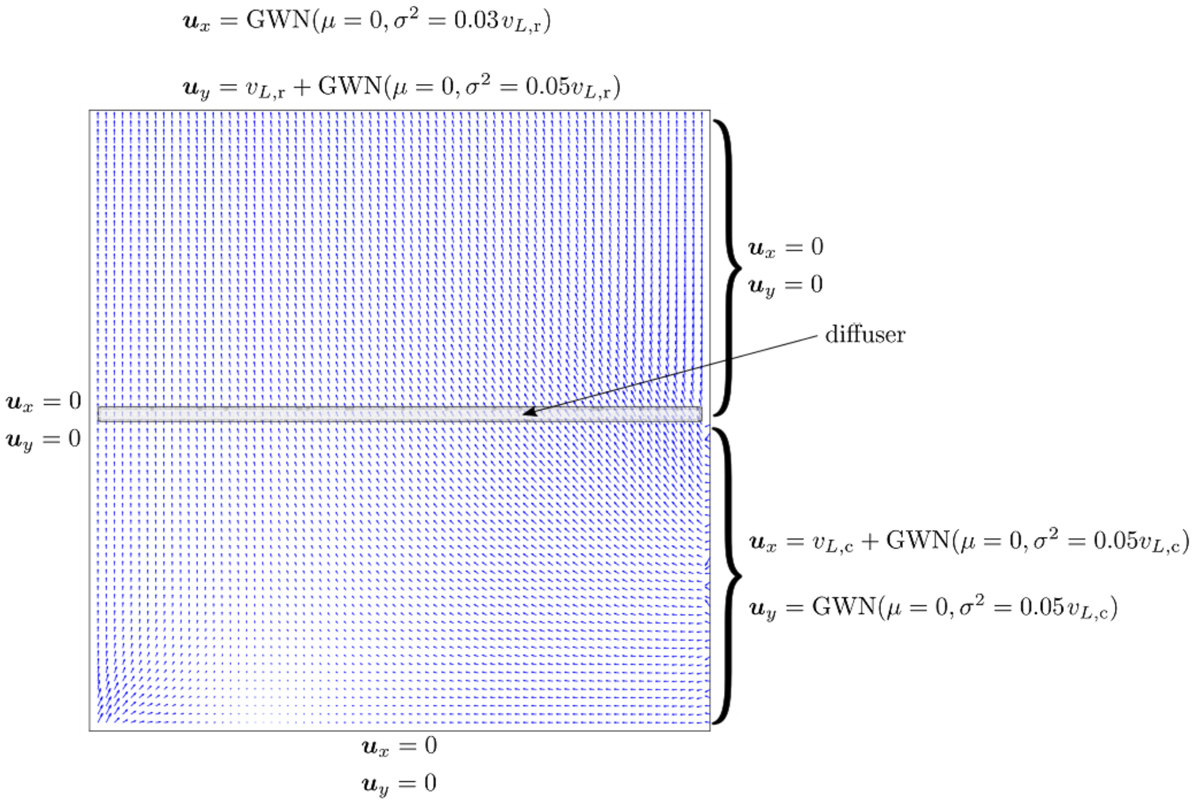

Figure 11: Velocity field at simulation starting time. The position of the diffuser assumed for this simulation is highlighted. For the sake of clarity, the grid is 150 × 150 instead of 300 × 300.

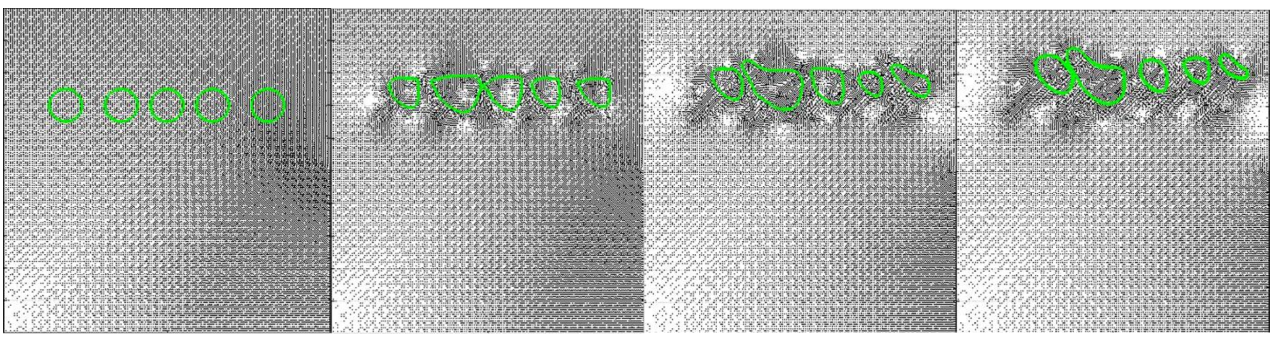

Figure 12. Simulation of instantaneous puff behavior for a 5 bubbles flow inside the riser, with CLSM.

3.5. Validation of the model and optimal growing conditions

The hydrodynamic experimental tests were carried out to investigate the three different regimes (bubble flow, transition or incipient churn, and churn) in the ALRs, in order to better characterize the incipient churn flow, i.e. the regime suggested in the literature for microalgae nurturing in ALRs [38,39] since it permits high Sh numbers without damaging the microalgae. In this regime the concomitant presence of large and small bubbles was experimentally observed, where the larger ones tend to slightly churn up the liquid while the smaller ones rise faster, stirring the liquid. The results of simulations using the modified level set method confirmed the trajectories of the churning bubbles at the corresponding conditions. Moreover, even if some adjustments need yet to be tested with the proposed CLSM, the modeled shape of the bubbles strongly corresponds (see the spherical caps in Figure 6b and Figure 9). So, the proposed model was used for the fine-tuning of the best-operating conditions in the ALRs. In particular, many simulations in the transition regime between bubble and churn were carried out. Different couples of Re numbers (respectively in the riser and in the downcomer) lead the ALRs into this transition regime, with the difference among them being the shape of the bubbles, which depends on the Eo number.

We choose an incipient churn regime with as similar as possible Re numbers in the two main sections of the reactor and with the requested shape for the bubbles, i.e. small spherical bubbles together with mainly spherical caps. These optimal conditions were kept in the outdoor cultivation tests (Table 5). The microalgae related parameters measured inside the ALRs, outdoor operated under these optimal hydrodynamic conditions, are also reported in Table 5 (and fully described in [2]).

Table: Growing conditions in the outdoor cultivation tests

Cultivation parameters	**Value**	**Hydrodynamics and mass transport parameters**	**Value**
CO_2 (%)	10	Re [downcomer]	11230
Glycerol (g L^{-1})	10	Re [riser]	10300

T (°C)	12 - 25	Sh [CO_2]	1400 - 1800
pH	7 - 9.5	liquid velocity [downcomer] (m s^{-1})	0.202
Conductivity (μS)	700 - 1200	liquid velocity [riser] (m s^{-1})	0.111
DO_x (mg L^{-1})	10 - 19	Gas velocity (bubbles) (m s^{-1})	0.585
I_0(μmol m^2 s^{-1})	1000 - 1680	Mean bubble diameter (m)	0.005
PFD (μmol m^2 s^{-1})	120 - 170	Bubbles in the riser	2200*
c_0 (g L^{-1}) initial, at each cycle	0.5	Average residence time (s)	26
c_f (g L^{-1}) at extraction	1.45 - 1.52	Gas flowrate (m^3 s^{-1})	0.0015

*the estimated experimental error is 22%

4. Conclusions

This paper dealt with the simulation of the bubble dynamics within the riser of an external loop airlift reactor, taking into account the geometry, and in particular the position of the sparger and the horizontal collectors. All the data used for validating simulation were collected or calculated from a set of experimental hydrodynamic campaigns on pilot-scale reactors. While classic CFD-based Euler-Euler and, sometimes, Euler-Lagrange methods have been extensively employed to model various types of reactors including bubble column ones, very few studies have been performed with front-tracking techniques, especially in conjunction with multiple, small bubbles. Therefore, we do not have many benchmarks for an effective comparison. These first results confirm the good ability of the level set method to manage the complex dynamics of multiphase systems. In particular, although simulating more bubbles at the same time, we identified bubble shapes coherent with those belonging to the classes found experimentally (spherical, ellipsoidal, dimpled ellipsoidal-cap, skirted, spherical-cap) in bubble, incipient churn, and churn regimes. Besides, the correct definition of the characteristics of the flow field highlighted the zig-zagging trajectories desired and obtained in the experimental tests. The physically-based model, after validation, was used for the fine-tuning of the regime inside the ALRs. The final suggested operating conditions for the outdoor cultivation tests entail Re numbers around 10000 - 11000, similar in all the sections of the ALRs; an Sh number in the range 1400 - 1800 and spherical-caps in the upper half of the riser, slightly churning the microalgae without damaging them. These conditions are reached by insufflating a flue gas flowrate of 0.0015 $m^3\ s^{-1}$ in each ALR.

Anticipated future developments concern, on the one hand, further optimization of the management of the computational domain and the reinitialization, and on the other hand the implementation of mass balance equations apt to simulate the absorption of CO_2 in the liquid, central for the growth of microalgae.

Funding: This research did not receive any specific grant from funding agencies in the public, commercial, or not-for-profit sectors.

Author contributions: MN, PB, OP Conceptualization; MN, PB Formal analysis; MN, PB, OP Investigation; MN, PB, OP Methodology; OP, PB Resources; MN Software; PB, OP Supervision; PB, OP Validation; MN, OP Writing - original draft; MN, PB, OP Writing - review &editing.

Notation

a	specific surface of the bubbles	$m^2\ m^{-3}$
A	cross-sectional area	m^2
d	signed distance function	m
d_b	equivalent diameter of a bubble	m
$\mathrm{d_c}$	diameter of the horizontal collectors of the ALR.	m
$\mathrm{d_r}$	diameter of the riser of the ALR.	m
D	diffusion coefficient	$m^2\ s^{-1}$

$\hat{\boldsymbol{e}}_g$	gravitational acceleration unit vector	-
g	gravitational acceleration	m s^{-2}
$\boldsymbol{g}$	gravity	m s^{-2}
H	Heaviside step function	-
H_ε	smoothed Heaviside function	-
k_L	liquid global mass transport coefficient	m s^{-1}
L	characteristic length	m
L_r	length of the riser	m
$\hat{\boldsymbol{n}}$	unit normal vector to the interface	-
p	pressure	Pa
t	time	s
T	convective time	s
u_G	gas velocity	m s^{-1}
$\boldsymbol{u}$	velocity	m s^{-1}
U	characteristic speed	m s^{-1}
$v_{L,\mathrm{c}}$	liquid mean velocity in the horizontal collector	m s^{-1}
$v_{L,\mathrm{r}}$	liquid mean velocity in the riser	m s^{-1}

$\boldsymbol{x}$	position vector	m
$\mathcal{S}$	modified signed function	m

Greek letters

$\delta(\phi)$	Dirac delta distribution	m^{-1}
$\delta_{\varepsilon}(\phi)$	mollified delta function	m^{-1}
ε	numerical smearing coefficient; interface thickness	-
ζ	volume viscosity	Pa s
κ	curvature	m^{-1}
Κ	level set method correction parameter	m
μ	dynamic viscosity	Pa s
ν	kinematic viscosity	$m^2\ s^{-1}$
$\boldsymbol{\xi}$	body force per unit volume	$N\ m^{-3}$
ϕ	standard level set function	m
ρ	mass density	$kg\ m^{-3}$
σ	surface tension coefficient	$N\ m^{-1}$
τ	artificial time	s
ψ	conservative level set function	m

Ω	computational domain	-
$\partial\Omega$	boundary between Ω^{+} and Ω^{-}	-

Dimensionless numbers

Eo	Eötvös number
Fr	Froude number
Mo	Morton number
Re	Reynolds number
Sh	Sherwood number

Subscripts and superscripts

$\star$	dimensionless
l	liquid phase
g	gas phase

Operators

$\frac{\partial}{\partial t}$	partial time derivative	s^{-1}
$\frac{\mathrm{D}}{\mathrm{D}t}$	substantial derivative	s^{-1}
$\boldsymbol{\nabla}$	gradient operator	m^{-1}
$\boldsymbol{\nabla}\cdot$	divergence operator	m^{-1}

$\boldsymbol{\Delta}$	Laplacian	m^{-2}

Supplementary Materials

S1. NSE non-dimensionalization

In section 2.2, a non-dimensional version of the NSE is presented. In the following, the procedure to obtain such a formulation is expounded.

To complete the non-dimensionalization of the NSE, as it is deducible from dimensional analysis, it is necessary to multiply both sides of Eq. (1) by the constant term $\mathrm{L}\,\mathrm{U}^{-2}$, hence obtaining the non-dimensionalized Navier–Stokes equations for an incompressible, isothermal, Newtonian fluid.

$$\frac{\mathrm{D}\boldsymbol{u}^\star}{\mathrm{D}t^\star} = -\boldsymbol{\nabla}^\star p^\star + \frac{g\mathrm{L}}{\mathrm{U}^2}\boldsymbol{g}^\star + \frac{\nu}{\mathrm{LU}}\Delta^\star\boldsymbol{u}^\star \tag{S.1}$$

As it is well known, for Newtonian, incompressible fluids, the continuity equation applies. It describes the velocity field $\boldsymbol{u}$ as a solenoidal vector field:

$$\boldsymbol{\nabla}\cdot\boldsymbol{u} = 0 \tag{S.2}$$

It follows that, if one considers $\boldsymbol{\xi} = \rho\boldsymbol{g}$ as it is often the case,

$$\frac{\mathrm{D}\boldsymbol{u}}{\mathrm{D}t} = -\frac{1}{\rho}\boldsymbol{\nabla}p + \boldsymbol{g} + \frac{\mu}{\rho}\Delta\boldsymbol{u} = -\frac{1}{\rho}\boldsymbol{\nabla}p + \boldsymbol{g} + \nu\Delta\boldsymbol{u} \tag{S.3}$$

having introduced the kinematic viscosity $\nu = \mu\,\rho^{-1}$ as well.

To perform non-dimensionalization, some scaling parameters are needed. One way to attack the problem [40] is to choose some characteristic length L and characteristic speed U and, exploiting gravitational acceleration g, to define suitable non-dimensional variables as follows:

$$\mathbf{x}^\star = \frac{\boldsymbol{x}}{\mathrm{L}},\quad \boldsymbol{u}^\star = \frac{\boldsymbol{u}}{\mathrm{U}},\quad \boldsymbol{g}^\star = \hat{\boldsymbol{e}}_g = \frac{\boldsymbol{g}}{g}$$

The selection of a proper pressure scale is not a foregone conclusion: a possibility, advisable for the cases in which dynamic effects are dominant, consists of obtaining the non-dimensional pressure $p^\star$ as the ratio $p\,\rho^{-1}\mathrm{U}^{-2}$. Besides, it is easy to observe how $\boldsymbol{\nabla}^\star = \mathrm{L}\boldsymbol{\nabla}$ and that the introduction of L and U naturally leads to the identification of the time scale, since

$$\mathrm{T} = \frac{\mathrm{L}}{\mathrm{U}} \tag{S.4}$$

where T is the convective time. It follows that one can define $t^\star$ as $t^\star = t\,\mathrm{T}^{-1}$.

L and U are adopted to assemble dimensionless quantities useful to analyze the similarity of different systems. For the similarity constraint to be satisfied, geometrical similarity, as well as similarity of boundary conditions and equality of each of these dimensionless groups are required. Generally speaking, characteristic physical quantities are liable to arbitrary choice, provided that they are well defined and referred to the same geometrical locations for every system [41].

Rearranging these latter mathematical expressions defining the non-dimensional quantities and plugging them in Eq. (S.3) leads to

$$\frac{\mathrm{U}^2}{\mathrm{L}}\frac{\mathrm{D}\boldsymbol{u}^\star}{\mathrm{D}t^\star} = -\frac{\rho\mathrm{U}^2}{L}\boldsymbol{\nabla}^\star p^\star\frac{1}{\rho} + g\boldsymbol{g}^\star + \nu\frac{\mathrm{U}}{\mathrm{L}^2}\Delta^\star\boldsymbol{u}^\star \tag{S.5}$$

being $\Delta^\star$ the non-dimensional Laplacian, i.e. the square of $\boldsymbol{\nabla}^\star$.

To complete the non-dimensionalization of the NSE, as it is deducible from dimensional analysis, it is necessary to multiply both sides of Eq. (S.5) by the constant term $\mathrm{L}\,\mathrm{U}^{-2}$, hence obtaining the non-dimensionalized Navier–Stokes equations for an incompressible, isothermal, Newtonian fluid.

$$\frac{\mathrm{D}\boldsymbol{u}^\star}{\mathrm{D}t^\star} = -\boldsymbol{\nabla}^\star p^\star + \frac{g\mathrm{L}}{\mathrm{U}^2}\boldsymbol{g}^\star + \frac{\nu}{\mathrm{LU}}\Delta^\star\boldsymbol{u}^\star \tag{S.6}$$

Two well-known similarity numbers, i.e. dimensionless groups, emerge in this way: the Reynolds number Re and Froude number Fr.

$$\mathrm{Re} = \frac{\mathrm{LU}}{\nu} \tag{S.7}$$

$$\mathrm{Fr} = \frac{\mathrm{U}}{\sqrt{g\mathrm{L}}} \tag{S.8}$$

Eq. (S.6) can, therefore, be condensed in

$$\frac{\mathrm{D}\boldsymbol{u}^{\star}}{\mathrm{D}t^{\star}} = \frac{\partial \boldsymbol{u}^{\star}}{\partial t^{\star}} + \boldsymbol{u}^{\star} \cdot \boldsymbol{\nabla}^{\star}\boldsymbol{u}^{\star} = -\boldsymbol{\nabla}^{\star}p^{\star} + \frac{1}{\mathrm{Fr}^2}\hat{\boldsymbol{e}}_g + \frac{1}{\mathrm{Re}}\Delta^{\star}\boldsymbol{u}^{\star} \tag{S.9}$$

S2. LSM details

LSM is a front capturing method, depicting a picture in which coordinates are fixed in space, i.e. an Eulerian method. From the perspective of the simulation of a system that involves bubble motion within a liquid domain and requires a high degree of precision considering the importance of their shape, Eulerian methods seem to be preferable. In fact, having an external stationary reference frame at one’s disposal offers undeniable advantages in the delineation of bubble shape evolution: it enables one to take into account topology variations whereby bubbles may coalesce and break up. Moreover, Lagrangian methods prove to be ill-suited to cope with such problems since, while they preserve a sharp interface representation, they demand re-meshing when large deformations manifest and are subjected to mesh tangling and numerical inaccuracy due to highly irregular meshes [42], being prone to blow up.

Among other virtues of LSM, its ability to naturally determine intrinsic geometrical properties of the moving interfaces such as their normal vector $\hat{\boldsymbol{n}}$ turns out to be very advantageous also in the perspective of dealing with physical properties such as surface tension. Simply by differentiation of ϕ, one is able to infer both $\hat{\boldsymbol{n}}$ and the curvature κ:

$$\hat{\boldsymbol{n}} = \frac{\boldsymbol{\nabla}\phi}{||\boldsymbol{\nabla}\phi||} \tag{S.10}$$

$$\kappa = \boldsymbol{\nabla} \cdot \hat{\boldsymbol{n}} \tag{S.11}$$

S2.1. On LSM reinitialization

ϕ is generally initialized into the signed distance function $d(\boldsymbol{x}, t) = \min_{\boldsymbol{x}_{\partial\Omega} \in \partial\Omega} |\boldsymbol{x} - \boldsymbol{x}_{\partial\Omega}|$, with $\boldsymbol{x}_{\partial\Omega}$ being the closest point of the front from $\boldsymbol{x}$: in the probable event that the speed function $\boldsymbol{u}$ is not constant, ϕ can become either very flat or steep. Sussman et al. [43] proposed an iterative reinitialization of ϕ by reformulating $d(\boldsymbol{x}, t)$, i.e. the unique viscosity solution of the Eikonal equation $|\boldsymbol{\nabla}\phi| = 1$ anchored at ϕ_0, by solving another Hamilton-Jacobi PDE (Eq. (S.10)) in an artificial time reference τ.

$$\frac{\partial\phi(\boldsymbol{x}, t)}{\partial\tau} + \mathcal{S}(|\boldsymbol{\nabla}\phi(\boldsymbol{x}, t)| - 1) = 0 \tag{S.12}$$

where $\mathcal{S}$ is a modified signed function [44]. Albeit subject to CFL limitations, this procedure is widely employed as it translates into an accurate reconstruction of the distance profile.

The application of LSM to fluid dynamic problems hinges on three mathematical functions: other than the level set function ϕ, Dirac delta δ and Heaviside step function H play a crucial role. Even though the thickness of the interface may be inconsiderable from a physical perspective, LSM calls for the prescription of a fixed and numerically relevant front thickness as a means to alleviate numerical difficulties that may arise due to sharp changes of the considered physical properties across $\partial\Omega$. To avoid jump discontinuities, sharp changes in the properties of Ω^+ and Ω^- regions are smudged by the means of a smoothed Heaviside function $H_\varepsilon(\phi)$, whilst mollified delta function $\delta_\varepsilon(\phi)$ is employed to analogously model the surface tension force [45]. Specifically, Osher and Fedkiw [46] report the definition of $H_\varepsilon(\phi)$ as

$$H_\varepsilon(\phi) = \begin{cases} 0 & \phi < -\varepsilon \\ \dfrac{1}{2} + \dfrac{\phi}{2\varepsilon} + \dfrac{1}{2}\sin\left(\dfrac{\pi\phi}{\varepsilon}\right) & -\varepsilon \le \phi \le \varepsilon \\ 1 & \varepsilon < \phi \end{cases} \tag{S.13}$$

where ε is a parameter influencing the numerical smearing and usually of the same order of magnitude as the interface thickness, and $\delta_\varepsilon(\phi)$ as its derivative:

$$\delta_\varepsilon(\phi) = \begin{cases} 0 & \phi < -\varepsilon \\ \dfrac{1}{2\varepsilon} + \dfrac{1}{2\varepsilon}\cos\left(\dfrac{\pi\phi}{\varepsilon}\right) & -\varepsilon \le \phi \le \varepsilon \\ 1 & \varepsilon < \phi \end{cases} \tag{S.14}$$

References

[1] E. Brutschin, A. Fleig, Geopolitically induced investments in biofuels, Energy Econ. 74 (2018) 721–732. https://doi.org/10.1016/j.eneco.2018.06.013.

[2] O. Paladino, M. Neviani, Airlift photo-bioreactors for Chlorella vulgaris cultivation in closed-loop zero waste biorefineries, Biomass Bioenergy. 144 (2021) 105926. https://doi.org/10.1016/j.biombioe.2020.105926.

[3] J.-Y. Park, M.S. Park, Y.-C. Lee, J.-W. Yang, Advances in direct transesterification of algal oils from wet biomass, Bioresour. Technol. 184 (2015) 267–275. https://doi.org/10.1016/j.biortech.2014.10.089.

[4] W.N.A. Kadir, M.K. Lam, Y. Uemura, J.W. Lim, K.T. Lee, Harvesting and pre-treatment of microalgae cultivated in wastewater for biodiesel production: A review, Energy Convers. Manag. 171 (2018) 1416–1429. https://doi.org/10.1016/j.enconman.2018.06.074.

[5] R. Davis, A. Aden, P.T. Pienkos, Techno-economic analysis of autotrophic microalgae for fuel production, Appl. Energy. 88 (2011) 3524–3531. https://doi.org/10.1016/j.apenergy.2011.04.018.

[6] J. Kim, G. Yoo, H. Lee, J. Lim, K. Kim, C.W. Kim, M.S. Park, J.-W. Yang, Methods of downstream processing for the production of biodiesel from microalgae, Biotechnol. Adv. 31 (2013) 862–876. https://doi.org/10.1016/j.biotechadv.2013.04.006.

[7] L. Moreno-Garcia, K. Adjallé, S. Barnabé, G.S.V. Raghavan, Microalgae biomass production for a biorefinery system: Recent advances and the way towards sustainability, Renew. Sustain. Energy Rev. 76 (2017) 493–506. https://doi.org/10.1016/j.rser.2017.03.024.

[8] O. Paladino, M. Neviani, A closed loop biowaste to biofuel integrated process fed with waste frying oil, organic waste and algal biomass: Feasibility at pilot scale, Renew. Energy. 124 (2018) 61–74. https://doi.org/10.1016/j.renene.2017.08.027.

[9] Y. Chisti, Biodiesel from microalgae, Biotechnol. Adv. 25 (2007) 294–306. https://doi.org/10.1016/j.biotechadv.2007.02.001.

[10] M. Mondal, S. Goswami, A. Ghosh, G. Oinam, O.N. Tiwari, P. Das, K. Gayen, M.K. Mandal, G.N. Halder, Production of biodiesel from microalgae through biological carbon capture: a review, 3 Biotech. 7 (2017) 99. https://doi.org/10.1007/s13205-017-0727-4.

[11] R. Sayre, Microalgae: The Potential for Carbon Capture, BioScience. 60 (2010) 722–727. https://doi.org/10.1525/bio.2010.60.9.9.

[12] S. Osher, J.A. Sethian, Fronts propagating with curvature-dependent speed: Algorithms based on Hamilton-Jacobi formulations, J. Comput. Phys. 79 (1988) 12–49. https://doi.org/10.1016/0021-9991(88)90002-2.
[13] O. Paladino, M. Neviani, Scale-up of photo-bioreactors for microalgae cultivation by π-theorem, Biochem. Eng. J. 153 (2020) 107398. https://doi.org/10.1016/j.bej.2019.107398.
[14] M. Hamood-ur-Rehman, F. Ein-Mozaffari, Y. Dahman, Dynamic and local gas holdup studies in external loop recirculating airlift reactor with two rolls of fiberglass packing using electrical resistance tomography, J. Chem. Technol. Biotechnol. 88 (2013) 887–896. https://doi.org/10.1002/jctb.3917.
[15] M. Massabò, F. Catania, O. Paladino, A New Method for Laboratory Estimation of the Transverse Dispersion Coefficient, Groundwater. 45 (n.d.) 339–347. https://doi.org/10.1111/j.1745-6584.2007.00301.x.
[16] O. Paladino, F. Fissore, M. Neviani, A Low-Cost Monitoring System and Operating Database for Quality Control in Small Food Processing Industry, J. Sens. Actuator Netw. 8 (2019) 52. https://doi.org/10.3390/jsan8040052.
[17] E.W. Becker, Microalgae: Biotechnology and Microbiology, Cambridge University Press, 1994.
[18] A. Sadeghizadeh, F. Farhad dad, L. Moghaddasi, R. Rahimi, CO2 capture from air by Chlorella vulgaris microalgae in an airlift photobioreactor, Bioresour. Technol. 243 (2017) 441–447. https://doi.org/10.1016/j.biortech.2017.06.147.
[19] I.T.D. Cabanelas, Z. Arbib, F.A. Chinalia, C.O. Souza, J.A. Perales, P.F. Almeida, J.I. Druzian, I.A. Nascimento, From waste to energy: Microalgae production in wastewater and glycerol, Appl. Energy. 109 (2013) 283–290. https://doi.org/10.1016/j.apenergy.2013.04.023.
[20] G.K. Batchelor, An Introduction to Fluid Dynamics, Cambridge University Press, 2000.
[21] A.J. Chorin, J.E. Marsden, A Mathematical Introduction to Fluid Mechanics, 2nd ed., Springer-Verlag, New York, 1990.
[22] J.U. Brackbill, D.B. Kothe, C. Zemach, A continuum method for modeling surface tension, J. Comput. Phys. 100 (1992) 335–354. https://doi.org/10.1016/0021-9991(92)90240-Y.
[23] B. Seibold, A compact and fast Matlab code solving the incompressible Navier-Stokes equations on rectangular domains, (2008). http://math.mit.edu/~gs/cse/codes/mit18086_navierstokes.pdf.
[24] I.M. Mitchell, The Flexible, Extensible and Efficient Toolbox of Level Set Methods, J. Sci. Comput. 35 (2008) 300–329. https://doi.org/10.1007/s10915-007-9174-4.
[25] H. Abdulmouti, Bubbly Two-Phase Flow: Part I- Characteristics, Structures, Behaviors and Flow Patterns, Am. J. Fluid Dyn. 4 (2014) 194–240.
[26] R. Krishna, J.M. Van Baten, Scaling up Bubble Column Reactors with the Aid of CFD, Chem. Eng. Res. Des. 79 (2001) 283–309. https://doi.org/10.1205/026387601750281815.
[27] J.R. Grace, Shapes and Velocities of Bubbles Rising in Infinite Liquids, Trans. Inst. Chem. Eng. 51 (1973) 116–120.
[28] R.A. Bello, C.W. Robinson, M. Moo-Young, Prediction of the volumetric mass transfer coefficient in pneumatic contactors, Chem. Eng. Sci. 40 (1985) 53–58. https://doi.org/10.1016/0009-2509(85)85046-6.
[29] A. Smolianski, Numerical modeling of two-fluid interfacial flows, Ph.D. Thesis, University of Jyväskylä, 2001.
[30] O. Paladino, G. Hodaifa, M. Neviani, M. Seyedsalehi, A. Malvis, Chapter 11 - Modeling in environmental interfaces, in: G.Z. Kyzas, A.C. Mitropoulos (Eds.), Interface Sci. Technol., Elsevier, 2019: pp. 241–282. https://doi.org/10.1016/B978-0-12-814178-6.00011-X.
[31] E. Olsson, G. Kreiss, A conservative level set method for two phase flow, J. Comput. Phys. 210 (2005) 225–246. https://doi.org/10.1016/j.jcp.2005.04.007.
[32] E. Olsson, G. Kreiss, S. Zahedi, A conservative level set method for two phase flow II, J. Comput. Phys. 225 (2007) 785–807. https://doi.org/10.1016/j.jcp.2006.12.027.

[33] T. Waclawczyk, A consistent solution of the reinitialization equation in the conservative level-set method, J. Comput. Phys. 299 (2015) 487–525. https://doi.org/10.1016/j.jcp.2015.06.029.
[34] R. Chiodi, O. Desjardins, A reformulation of the conservative level set reinitialization equation for accurate and robust simulation of complex multiphase flows, J. Comput. Phys. 343 (2017) 186–200. https://doi.org/10.1016/j.jcp.2017.04.053.
[35] J.O. McCaslin, O. Desjardins, A localized re-initialization equation for the conservative level set method, J. Comput. Phys. 262 (2014) 408–426. https://doi.org/10.1016/j.jcp.2014.01.017.
[36] O. Desjardins, V. Moureau, H. Pitsch, An accurate conservative level set/ghost fluid method for simulating turbulent atomization, J. Comput. Phys. 227 (2008) 8395–8416. https://doi.org/10.1016/j.jcp.2008.05.027.
[37] P. Bagnerini, M. Neviani, O. Paladino, Simulation of the rising of gas bubbles in a pilot-scale external loop airlift photobioreactor, E3S Web Conf. 113 (2019) 03023. https://doi.org/10.1051/e3sconf/201911303023.
[38] A. Kommareddy, G. Anderson, S. Gent, G. Bari, The impact of air flow rate on photobioreactor sparger/diffuser bubble size(s) and distribution, in: Proc. Am. Soc. Agric. Biol. Eng. Annu. Int. Meet. 2013, ASABE, Kansas City, Missouri, 2013. http://dx.doi.org/10.13031/aim.20131620764.
[39] J.P. Bitog, I.-B. Lee, C.-G. Lee, K.-S. Kim, H.-S. Hwang, S.-W. Hong, I.-H. Seo, K.-S. Kwon, E. Mostafa, Application of computational fluid dynamics for modeling and designing photobioreactors for microalgae production: A review, Comput. Electron. Agric. 76 (2011) 131–147. https://doi.org/10.1016/j.compag.2011.01.015.
[40] R.W. Fox, A.T. McDonald, P.J. Pritchard, Introduction to Fluid Mechanics, 6th ed., Wiley, Hoboken, NJ, 2005.
[41] D. Pnueli, C. Gutfinger, Fluid Mechanics, Cambridge University Press, 1997.
[42] J.K. Dukowicz, Lagrangian fluid dynamics using the Voronoi-Delauanay mesh, Los Alamos Scientific Lab., Los Alamos, NM, 1981. http://inis.iaea.org/Search/search.aspx?orig_q=RN:12636166.
[43] M. Sussman, P. Smereka, S. Osher, A Level Set Approach for Computing Solutions to Incompressible Two-Phase Flow, J. Comput. Phys. 114 (1994) 146–159. https://doi.org/10.1006/jcph.1994.1155.
[44] D. Hartmann, M. Meinke, W. Schröder, Differential equation based constrained reinitialization for level set methods, J. Comput. Phys. 227 (2008) 6821–6845. https://doi.org/10.1016/j.jcp.2008.03.040.
[45] A. Sharma, Level set method for computational multi-fluid dynamics: A review on developments, applications and analysis, Sadhana. 40 (2015) 627–652. https://doi.org/10.1007/s12046-014-0329-3.
[46] S. Osher, R. Fedkiw, Level Set Methods and Dynamic Implicit Surfaces, Springer-Verlag, New York, 2003. //www.springer.com/gp/book/9780387954820 (accessed April 4, 2018).

CAPTIONS

Figures

Figure 1. External loop airlift reactor: A – riser; B – downcomer; C – horizontal collectors.

Figure 2. Illustration of the LSM.

Figure 3. Numerical model schematization.

Figure 4. Staggered grid with boundary cells.

Figure 5. Grace's diagram [40]

Figure 6. Bubbles in the riser from the experimental campaign in incipient churn flow: (a) bubble flow (gas bubble velocity = 0.12 m s^{-1}); (b) transition (gas bubble velocity=0.35 m s-1); (c) churn flow (gas bubble velocity = 0.62 m s^{-1})

Figure 13. Simulation frames of the single bubble dynamic in the riser with LSM modified by the relocation of the level set function using the bisection method. On the background, the speed plot of the liquid velocity field; vectors are auto-scaled as to not overlap.

Figure 14. Level set correction by the relocation of the level set function ϕ, translated upward or downward by a signed constant K.

Figure 15. Simulation frames of instantaneous puff behavior for a 5 bubbles flow inside the riser, with LSM modified by the relocation of the level set function using the bisection method. To obtain a clearer and more understandable picture of bubble dynamics, the quiver plot has been disabled.

Figure 10. Comparison between standard LS (top) and Conservative LS (bottom) functions.

Figure 11: CLS function remapping.

Figure 12: Velocity field at simulation starting time. The position of the diffuser assumed for this simulation is highlighted. For the sake of clarity, the grid is 150 × 150 instead of 300 × 300.

Figure 13. Simulation of instantaneous puff behavior for a 5 bubbles flow inside the riser, with CLSM.

Tables

Table 1. Physical-chemical data used in the simulation.

Table 2. Data gathered in the experimental campaigns.

Table 3: Ranges of variables experimentally determined in ALRs.

Table 4: Ranges of variables calculated with empirical correlations and related dimensionless numbers in ALRs.

Table 5: Growing conditions in the outdoor cultivation tests